Self-assembled patterns from evaporating layered fluids

L V Govor[1], J Parisi[1], G H Bauer[1] and G Reiter[2]

[1] Institute of Physics, University of Oldenburg, D-26111 Oldenburg, Germany
[2] Institute of Physics, University of Freiburg, D-79104 Freiburg, Germany

E-mail: leonid.govor@uni-oldenburg.de

Abstract
We studied the formation of tree-like patterns of polymer aggregates and rings of nanoparticles during evaporation from a fluid film. We utilize phase separation between two immiscible fluids to generate a double-layer film which dries up in a sequential manner. Both fluid layers may contain a solute, polymer aggregates or nanoparticles. During evaporation of the top layer, instabilities may occur and direct a self-assembly process of the solute which may be further affected by an instability of the bottom layer at a later stage. We present two cases where, after evaporation of the top fluid layer, the solute was adsorbed on the surface of the bottom fluid layer. In comparison to dewetting of a single fluid layer on a solid substrate, the advantage of our double-layer approach lies in the deposition of the solute on the surface of the bottom fluid layer. The relatively high mobility of the solute on such a fluid surface favors the formation of ordered patterns, driven by an instability of the bottom layer.

1. Introduction

Evaporation of the solvent from polymer solution films on a solid substrate may have a large influence on the resulting film morphology. The basic behavior of thin liquid films located on solid substrates is already well understood. Several instability mechanisms are known that can destabilize an initially flat liquid film (one-layer system) and were investigated in a large number of experimental [1–5] and theoretical [6–14] works. The stability of liquid films with a thickness below 100 nm, deposited on a substrate, is governed by the effective molecular interactions at the interface between substrate and surface of the layer, for instance, by long-range van der Waals and short-range electrostatic forces [15]. After deposition on partially wettable solid substrates, these liquid films may become unstable and often dewet by forming holes. According to theory, the film instability followed by dewetting occurs when the second derivative of the excess intermolecular interaction energy per unit area with respect to the film thickness becomes negative [11].

When a thin film consisting of two layers of immiscible liquids is deposited on a solid substrate, a more complicated situation appears. In such a two-layer system (double layer), one discloses a richer dynamics compared to that for one-layer systems, as both liquid–liquid and liquid–gas interfaces evolve in a coupled way. Instability phenomena will be driven by the effective molecular interactions acting between each of the three interfaces which separate the four media: substrate, bottom layer, top layer and surrounding gas (air). Only a few theoretical investigations exist on the stability of a bilayer composed of two superposed thin films of nonvolatile fluids deposited on a solid substrate [16, 17]. However, instability phenomena arising in the course of drying of a double-layer system (solvent evaporation) have practically never been studied.

Recently we have presented an experimental study of instability phenomena developing in an evaporating double layer formed via phase separation in a thin film of mixed polymer solutions. There, solvent evaporation from two layers led first to a decomposition of the top solution layer into micrometer-sized droplets, while the bottom layer did not become unstable and dried as a continuous film [18, 19]. In the present work, we show that the evaporation from a similar double layer may, in addition to a decay of the top layer into elongated solid aggregates, also be assembled into tree-like patterns by an instability of the bottom layer. The initial double layer consists of a poly(isobutyl methacrylate) (BMA) layer on top of a nitrocellulose (NC) solution layer. During evaporation, the top BMA layer becomes unstable and transforms into short solid ridges. Finally, the inhomogeneous evaporation of the

solvent from the NC solution layer connects the BMA ridges to tree-like patterns.

In a second example, we show that, by spreading of a hexane solution containing $CoPt_3$ particles, hexadecylamine and a little water on substrates coated with a NC thin layer, nanoparticles can be ordered into low-dimensional arrays. After spreading, such a binary solution film transforms into a double layer containing a hexane layer on top of a water layer. The hexane layer dewets the water layer, and the latter dewets the NC covered substrate. The relatively thick hexane layer dewets as a continuous film, while the relatively thin dewetting water layer decomposes into droplets. Finally, the particles follow the motion of the contact line of the dewetting water layer (i.e. the interface between air, water and substrate) and, thus, assemble into close-packed arrays at the periphery of the water droplets. As a general theme, in the present work, we show that the final ordering of a solute, which segregated into the interface with the underlying fluid layer in the course of solvent evaporation out of the top layer, is governed by the instability of the bottom layer.

2. Tree-like patterns formed in evaporating binary solution

2.1. Experimental details

In this experiment, we have used a binary mixture of solutions consisting of 0.05% NC (Aldrich, $M_r = 1.04$ kg mol^{-1}) in amyl acetate and of 0.05% BMA (Aldrich, molecular weight $M_w = 130$ kg mol^{-1}) in isopropanol. The binary solution was prepared via mixing these solutions at a volume ratio of 1:1. In the absence of polymers, amyl acetate and isopropanol are miscible. Amyl acetate dissolves nitrocellulose relatively well, but not so well poly(isobutyl methacrylate). On the other hand, isopropanol dissolves poly(isobutyl methacrylate) relatively well, but it is a non-solvent for nitrocellulose.

The prepared blend of solutions was spin-coated onto a glass substrate (12×16 mm^2; spin casting at 2000 rpm for 20 s). In the course of solvent evaporation (during spin coating), the thin layer of initially mixed solutions transformed into a double-layer structure which was composed of a layer containing mainly BMA at the solution–air interface. Isopropanol evaporated relatively fast and amyl acetate was not effectively dissolving BMA. In addition, BMA and NC did not mix. Thus, BMA tended to segregate to the interface of the (NC/amyl acetate) fluid layer, forming a layer mostly containing BMA which became unstable and led to the formation of aggregates on the surface of a layer of NC/amyl acetate. Finally, evaporation of the remaining solvent from the double layer assembled the BMA aggregates of the top layer into various patterns.

2.2. Tree-like patterns of polymer formed experimentally

After complete evaporation of both solvents from the thin film binary solution (spin-coated onto a glass substrate), various phase-separated patterns were observed, as imaged with a Dimension 3100 (Digital Instruments) atomic force microscope (AFM). Regions with tree-like patterns (figures 1(a) and (b)),
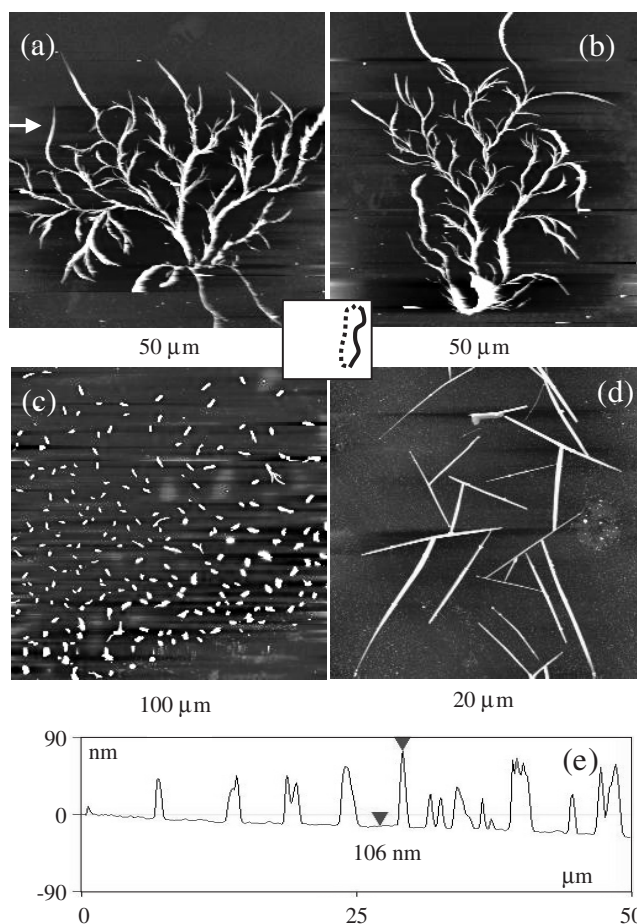

Figure 1. Tapping-mode AFM measurements: (a) height image of the tree-like branched structure; (b) height image of the structure located near the one shown in part (a); (c) height image of the region covered only with clusters; (d) height image of the BMA ridges; (e) profile analysis of the scan taken along the arrow indicated in (a). The vertical distance indicated in (e) amounts to 106 nm.

fragmented branches and aligned clusters (figure 1(c)), and individual ridges (figure 1(d)) of BMA were found on top of a thin NC film covering the entire glass substrate. The BMA patterns were located only in a small part of the sample—along the edge (solid line in the inset of figure 1) of the curved stripe with a width of about 300 μm, extending over a length of about 8 mm—which represents the area where the evaporation and dewetting process of the top layer has led to the deposition of BMA aggregates. The size of the branched patterns varied from a few tens to about 150 μm and the corresponding height from a few tens to about 120 nm (figure 1(e)). The length, width and thickness of the aligned clusters at one boundary of the stripe (solid line in the inset of figure 1) on average amounted to 5 μm, 1 μm and 120 nm, respectively. The size of these clusters decreases in direction to the other boundary of the stripe (dotted line). The BMA ridges could be observed as individual objects on the NC film or they may interconnect under various angles. The length of these ridges varied from 3 to 10 μm, the width extended from 0.2 to 1 μm and the thickness ranged from 20 to 50 nm. The particular feature of the pattern illustrated in figure 2(a) (lower part) is
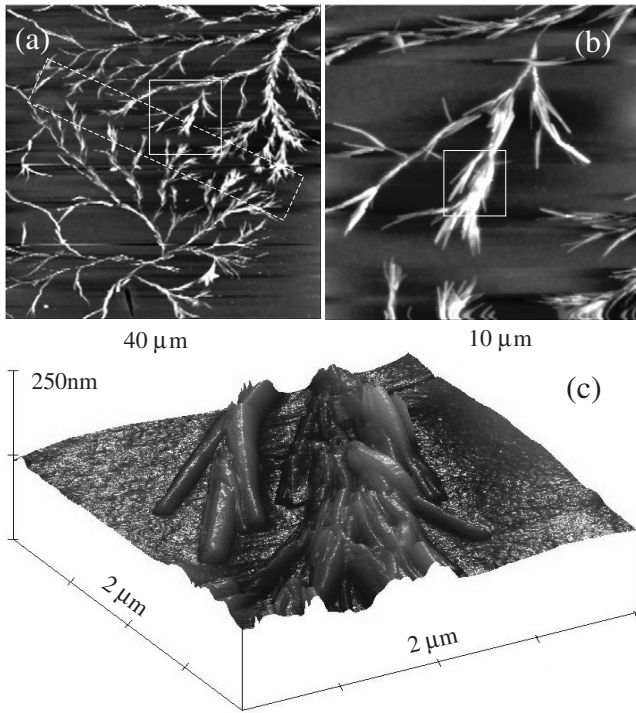
Figure 2. Tapping-mode AFM measurements: (a) height image of adjacent tree-like structures separated by a border (indicated by the dashed box); (b) magnified image of an area indicated by the square box (solid line) in (a); (c) three-dimensional magnified image of a branch indicated by the box in (b).

an ordering of some such branches into a wreath. Moreover, between adjacent tree-like structures, a clearly detectable border zone existed (indicated by the dashed box in figure 2(a)) extending to a few μm, where no ridges were deposited. The details of an individual branch of such tree-like structures, illustrated in figures 2(b) and (c), indicate that these consisted of a tangle of several BMA ridges.

For a detailed understanding of the mechanisms which led to the formation of the above structures, we have determined the penetration depth of the BMA branches into the underlying NC film. For this purpose, the BMA structures were removed by immersing the specimen in a bath of isopropanol (120 min; 60 °C), since isopropanol is not a solvent for NC. The depressions remaining in the NC film after removal of the BMA branches were about 5 nm deep. The thickness of the NC film directly under the BMA branches also amounted to about 5 nm. This means that the BMA branches had no contact with the substrate, which supports our previous conclusion that during the evaporation process the initial film of mixed solutions transformed into a double-layer structure which consisted of a BMA solution layer on top of an NC solution layer.

2.3. Instabilities developing in evaporating double layer

Isopropanol dissolves only BMA but not NC. As isopropanol has a lower surface tension than amyl acetate, BMA has a lower surface tension than NC and amyl acetate can slightly dissolve BMA, we conclude that, at a rather early stage of solvent

evaporation, the system will separate into a surface layer rich in BMA and one close to the substrate rich in NC. For simplicity, we assume that the above separation into a double layer occurs already at a very early stage. Under this assumption, we can proceed with the following qualitative discussion, which reflects the basic processes.

The total thickness of the solution film prepared by spin-coating was of the order of 1 μm, i.e. a BMA solution layer and the NC solution layer were each roughly about 0.5 μm thick. The BMA solution wetted the layer of the NC solution, if the spreading coefficient $S_{21} = \gamma_1 - \gamma_2 - \gamma_{21}$ was positive [20]. Here, γ_2 and γ_1 designate the surface tension of the BMA solution and that of the NC solution (at the boundary to air), respectively; γ_{21} is the interfacial tension between BMA and NC solution. For discussing the alteration of both parameters γ_2 and γ_1 during evaporation, we have experimentally determined the evaporation rates of isopropanol and amyl acetate from the surface of a Petri dish which amount to $(5.8 \pm 0.2) \times 10^{-2}$ mg s^{-1} and $(1.2 \pm 0.2) \times 10^{-2}$ mg s^{-1}, respectively [21].

The time dependence of both the thickness $d_2(t)$ and the surface tension $\gamma_2(t)$ of the BMA solution layer were determined from the evaporation rate of isopropanol in the two-phase solvent. The corresponding dependences $d_1(t)$ and $\gamma_1(t)$ can be obtained for the NC solution layer (figure 3). For the complete evaporation of isopropanol from the layer with $d_2 = 500$ nm, we get the time $t_2 = 1.35$ s, and for an amyl acetate layer with $d_1 = 500$ nm, $t_1 = 7.15$ s. For each solvent, the remaining mass during evaporation between $0 < t < t_0$ can be described as $m_s = m_{s0}(1 - t/t_0)$, where m_{s0} denotes the mass of isopropanol or amyl acetate at $t = 0$. In summary, we have determined $m_{s0} = m_{I0}$ and $t_0 = t_2$ for isopropanol, as well as $m_{s0} = m_{A0}$ and $t_0 = t_1$ for amyl acetate. In a first approximation, we can consider that surface tension $\gamma_2(t)$ of the solution that contains isopropanol (γ_I) and BMA (γ_{BMA}) can be described by a linear combination of solvent and polymer surface tension [20, 22–24]:

$$\gamma_2 = \gamma_I N_I + \gamma_{BMA} N_{BMA} - \beta N_I N_{BMA}, \qquad (1)$$

where β is a semi-empirical constant. $N_I = (1 - t/t_2)/(1 - t/t_2 + \alpha)$ and $N_{BMA} = \alpha/(1 - t/t_2 + \alpha)$ are fractions of the corresponding components in the solution, where $\alpha = m_{BMA}/m_{I0}$ and m_{BMA} denotes the mass of BMA in the top layer. Accordingly, equation (1) can be used for the NC solution that contains amyl acetate and NC. Figure 3(b) displays the results calculated for both surface tensions $\gamma_2(t)$ and $\gamma_1(t)$ versus evaporation time t. The corresponding spreading coefficients S_{21} and S_{1G} (spreading of the NC solution on the glass substrate) versus evaporation time are outlined in figure 3(c). The interfacial tensions γ_{21} and γ_{1G} were calculated following Israelachvili [15]. For instance, $\gamma_{21} \approx \gamma_2 + \gamma_1 - 2(\gamma_{2d}\gamma_{1d})^{0.5} - 2(\gamma_{2p}\gamma_{1p})^{0.5}$, where γ_{2d}, γ_{1d} and γ_{2p}, γ_{1p} are the dispersive and polar components of the surface tensions γ_2 and γ_1, respectively. So far, no experimental results are available allowing us to separate these two components and, thus, the values γ_2 and γ_1 were used for the estimation of γ_{21}, i.e. $\gamma_{21} \approx \gamma_2 + \gamma_1 - 2(\gamma_2\gamma_1)^{0.5}$. Accordingly, the
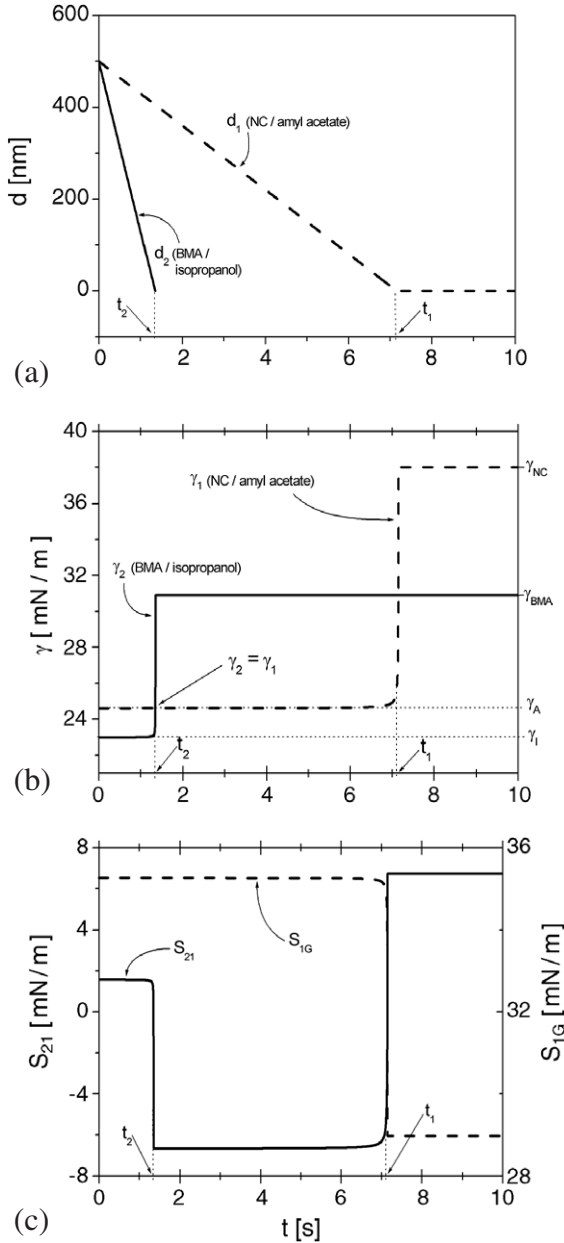
Figure 3. (a) Calculated thickness of both BMA solution (d_2) and NC solution (d_1) layers as a function of evaporation time. (b) Calculated surface tension versus evaporation time of the binary polymer solution. The curve $\gamma_2(t)$ characterizes the evaporation process of the BMA solution layer with $\gamma_I = 23.0$ mN m^{-1} (isopropanol), $\gamma_{BMA} = 30.9$ mN m^{-1} (poly(isobutyl methacrylate)), $m_{I0} = 7.9 \times 10^{-2}$ mg, $m_{BMA} = 0.5 \times 10^{-4}$ mg and $\beta = 1$ mN m^{-1}. The curve $\gamma_1(t)$ describes the evaporation of the NC solution layer with $\gamma_A = 24.6$ mN m^{-1} (amyl acetate), $\gamma_{NC} = 38$ mN m^{-1} (nitrocellulose), $m_{A0} = 8.8 \times 10^{-2}$ mg, $m_{NC} = 0.5 \times 10^{-4}$ mg and $\beta = 1$ mN m^{-1}. Values of γ_{NC}, γ_{BMA}, γ_A and γ_I are indicated additionally on the right-hand side, respectively. (c) Calculated spreading coefficients S_{21} and S_{1G} as a function of evaporation time.

dependences $S_{21}(t)$ and $S_{1G}(t)$ illustrated in figure 3(c) should be considered as qualitative indicators.

From results illustrated in figure 3(c), we deduce that during evaporation $S_{21} > 0$ until $\gamma_2 = \gamma_1$, i.e. in the time span from 0 to approximately 1.35 s. Only for $S_{21} < 0$, i.e. for 1.35 s $< t <$ 7.15 s, the top BMA layer may become unstable

and, thus, may dewet the underlying NC solution layer. In contrast, the NC solution layer remains stable during this stage, because S_{1G} is always positive (figure 3(c)). Here, we used $\gamma_G = 72.5$ mN m^{-1} for the surface tension of hydrophilic glass [15]. From results in figure 3(a), we deduce at $t \approx 1.35$ s the thickness amounts to $d_2 \approx 10$ nm, while $d_1 \approx 400$ nm. Dewetting of the BMA solution layer on the surface of the NC solution layer leads to a decrease of the area of the former one and to a corresponding increase of its height. In accordance with the experimental result shown in figure 1(d), we conclude that dewetting of the BMA solution layer led to the formation of fingers at the periphery of this layer (dewetting front, i.e. the three-phase contact line where the BMA and NC solution layers are simultaneously in contact with air) in a similar way as observed for dewetting of a polymer solution on a solid substrate [25]. We believe that the main mechanism driving this fingering instability is related to the gradients in polymer concentration and surface tension close to the three-phase contact line caused by solvent evaporation [26]. During the dewetting process, these fingers form long ridges of the BMA solution on the surface of the NC solution layer.

Before solvent evaporation has been completed from the long ridges of the BMA solution, these ridges are still highly deformable and may decompose into much shorter ridges or droplets accordingly with the well-known Rayleigh instability. By considering small sinusoidal perturbations on a liquid cylinder of radius r_c, Rayleigh [27] found that there is an optimum wavelength, $\lambda_R \approx 9r_c$, for which perturbations grow fastest, leading to the decomposition of a liquid cylinder into a chain of droplets. For the Rayleigh instability, the characteristic time τ_R over which perturbations grow and eventually break the long ridges of the BMA solution is given by a balance of surface tension and inertia:

$$\tau_{R,i} = (r_c^3 \rho_2 / \gamma_2)^{0.5}, \qquad (2)$$

where ρ_2 is the density and γ_2 is the surface tension of the BMA solution [28]. If the viscosity of the solution η_2 becomes important, we may approximate the characteristic time by [29]

$$\tau_{R,v} = r_c \eta_2 / \gamma_2. \qquad (3)$$

In both cases, for ridges in the range of some micrometers, τ_R is rather short, i.e. of the order ranging from microseconds to milliseconds. Thus, time τ_R is small compared to the total time span during which the BMA layer on top of the NC solution layer is in the unstable regime. After complete solvent evaporation of isopropanol, the BMA ridges become solid and remain on a fluid NC solution layer.

2.4. Scenario of the tree-like pattern formation

According to the experimental results described above, we assume that the BMA ridges are connected to a tree-like pattern during the inhomogeneous solvent evaporation from the NC solution layer. The formation of such patterns is only possible within the time interval determined by the expenditure necessary to first evaporate isopropanol and

finally amyl acetate from the film (i.e. 1.35 s and 7.15 s, respectively, see figure 3), where the NC solution layer remains liquid and the BMA ridges are mobile. The existence of a pronounced boundary between the adjacent tree-like structures illustrated in figure 2(a) (dashed box) indicates that, during solvent evaporation, several independent solidification domains appeared simultaneously which grew as the consequence of the formation of dry patches nucleated within the NC solution layer. As an example, figure 4(a) schematically shows the appearance of two such solidification domains A and B (denoted by dotted lines which advance in the course of the drying process) within the NC solution layer whose surface is covered with BMA ridges. The point s_A denotes the starting point for the solidification domain A within the NC solution layer. The corresponding point of domain B is located outside the figure. Both domains are close to each another, but their solidification fronts (i.e. the interface between the still fluid and the already dry NC layer) move in different directions denoted by the small arrows in figure 4(a). That means each solidification domain may be characterized by the particular motion of its solidification front that leads to some ordering of the BMA ridges into individual structures. The initial step of such ordering is illustrated in figure 4(a). Figure 3(b) demonstrates that solvent evaporation from the NC solidification domain is characterized by $d\gamma_1/dc < 0$ (c gives the concentration of the evaporating solvent). In this case, the solvent evaporation from the wedge-shaped region near the solidification front leads to a liquid flow directed from thicker parts of the NC solution layer to its thinner ones [30]. In figure 4(a), the direction of the flow motion is denoted by the wide arrows. The BMA ridges located on the surface of the liquid NC solution layer will be dragged along by the flow of the NC solution, and their velocity may be proportional to the gradient in the surface tension resulting from the increase of the concentration of NC upon approaching the solidification front. A few exemplary solidification fronts (representing different points in time during the drying of the NC layer) of domains A and B are schematically illustrated as smooth convex lines in figure 4(b). Indeed, the motion of the solidification front is strongly influenced by fluctuations in the NC concentration and the NC solution thickness near the edge of the solidification domain. The latter can give rise to an instability of the solidification front and, correspondingly, cause (periodic) fluctuations, i.e. surface tension, layer thickness, radius of curvature and contact angle vary continuously along the solidification front. In other words, the various sectors of the solidification front move with different velocity. As a consequence, liquid flow from thicker parts of the NC solution layer to its solidification front acquires a complex form which is partially reflected in the way how BMA ridges are arranged into tree-like branched structures, as the NC solidification front moves (figure 4(b)). The experimentally observed distinct boundary (indicated by the dashed box in figure 2(a)) between the adjacent tree-like structures is in accordance with the model described above where the boundary results from a encounter of solidification
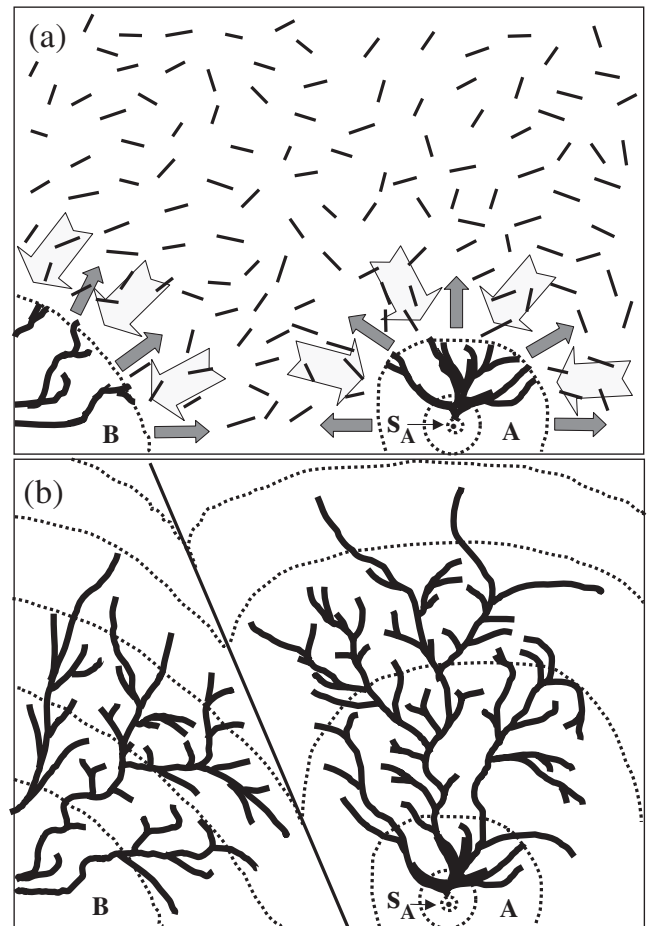

Figure 4. (a) Schematic illustration of a typical NC solidification domain A (on the right) appearing during solvent evaporation out of the NC solution layer. The domain A starts its growth at point s_A. The adjacent domain B (on the left) is indicated partially in the corner of the figure. The BMA ridges are illustrated as the short solid lines and solidification fronts as dotted lines. The small arrows at the solidification front indicate the direction of its motion, and the wide arrows the direction of the flow motion of BMA ridges.
(b) Schematic illustration of the outward motion of the solidification fronts of the domains A and B during the inhomogeneous solvent evaporation leading to the connection of BMA ridges into a tree-like pattern. The solid line illustrates a border where the solidification fronts of both the domains A and B coalesce.

fronts of adjacent domains (see the boundary between domains A and B illustrated by a solid line in figure 4(b)).

In summary, it has been demonstrated experimentally that phase separation of a binary solution appearing during the spin-coating deposition process can lead to pattern formation resulting from the solidification of an immiscible solute from a top fluid layer. These solid aggregates are floating on a longer-lived bottom fluid layer. Finally, the drying of the bottom layer drives the assembly of the solid aggregates into tree-like patterns. In the following second example, we present a similar double-layer system with solid nanoparticles already being present in the initial binary solution. We will show that also in such a case, the presence of an underlying fluid layer, which eventually becomes unstable and dewets, is favorable for the assembly of these nanoparticles.

3. Nanoparticle chains formed via a dewetting water layer

3.1. Experimental details

Hexane solutions with a particle concentration of 2.4×10^{12} and 3.1×10^{12} cm^{-3} of CoPt$_3$ (diameter 6 nm, stabilized with HDA [31]) were used in the present experiments. The corresponding values of volume concentration amount to $1.0 \times 10^{-5}\%$ and $1.3 \times 10^{-5}\%$, respectively. Additionally, HDA at a concentration 1.0×10^{-3} vol% and water at a concentration 1.0×10^{-2} vol% were added to the solution. Hexane itself contains a maximum 5×10^{-3} vol% of water (AppliChem GmbH), i.e. the total concentration of water in the solutions amounts to a maximum 1.5×10^{-2} vol%. In general, the solubility of water in hexane at 20 °C is 2.8×10^{-2} vol% [32] and, therefore, it was assumed that additional water was dissolved completely in the hexane solution of nanoparticles.

One drop of solution (3 μl) was cast either onto an Si substrate or a transmission electron microscopy (TEM) grid. Both substrates were covered with an NC film (thickness 100 nm). We found that the final patterns formed on both substrates were similar. The deposition radius $d_{s0} = 3.5$ mm of the spread solution layer remained constant for a time span of about 17 s and then quickly decreased toward the center of the spreading area. The total time span between the casting of the solution and its complete drying (hexane evaporation) amounted to about 20 s. At an early stage of the evaporation process, the solution layer transformed into a bilayer composed of a hexane layer on top of a water layer. The retraction (dewetting) of a comparatively thick hexane layer brought a thin water layer in contact with air. Due to the small initial amount of water, the resulting water layer was thin and became rapidly unstable leading to a decomposition into droplets, with the nanoparticles aligning at their periphery. Note, that the time span necessary for dewetting and final evaporation of the continuous hexane layer amounts to about 3 s, whereas the lifetime of the water droplets (as deduced from observation with an optical microscope) could be up to few minutes (for solutions without HDA). This time increased to a few days if the solution contained HDA. Similar droplet structures were formed in a closed desiccator in the presence of hygroscopic P$_2$O$_5$ powder, excluding the presence of water in air. Thus, the cooling of the substrate by hexane evaporation and possible condensation of water at ambient conditions did not play a significant role. Additionally, we found that the structure of water droplets did not substantially depend on the presence or absence of HDA in the solution. Accordingly, we conclude that, for an HDA concentration up to 0.001%, the process of phase separation of water in hexane only weakly depended on HDA.

The drying process of the solution layer on top of the NC/Si substrate was observed by a digital camera (Nikon Coolpix 995) mounted on an optical light microscope (magnification 200$\times$) recording 30 frames per second. Finally, after complete drying of the sample, the topography of the resulting structures on the NC-coated Si substrates or TEM grids were analyzed by AFM. For the films located on NC/TEM grids, the arrangement of the CoPt$_3$ particles was studied by TEM (Zeiss EM 902).

3.2. Nanoparticle arrays formed experimentally

A typical spatial and temporal evolution of the fluid solution film during its dewetting is shown in figure 5 for one sample of a total of nine equivalent studies [33]. It can be clearly seen that the dewetting system consists of two layers: the top hexane layer (h) dewets on the surface of the lower water layer (w), and that one dewets on the surface of the NC/Si substrate (s). During this two-stage dewetting process, the hexane layer stayed continuous (because it was comparatively thick), while the thin water layer deformed rapidly into a cellular structure that finally decomposed then into droplets. The dewetted distance ($d_{\rm h}$) of the hexane layer as a function of time t was measured at the edge of this layer. The resulting experimental dependence $d_{\rm h}(t)$ illustrated in figure 5(b) can be described as $d_{\rm h}(t) = P_{\rm h} t^{\alpha_h}$ with $\alpha_h = 1.15 \pm 0.01$. P_h is a time-independent prefactor. The temporal evolution of the dewetting water layer ($d_{\rm w}$) was determined via measurement of the diameter $D_{\rm w} = 2d_{\rm w}$ of the holes increasing with time (indicated by the dashed box and circle in figure 5(a)). The resulting dependence illustrated in figure 5(c) can be described as $d_{\rm w}(t) = P_w t^{\alpha_{\rm w}}$ with $\alpha_{\rm w} = 0.75 \pm 0.02$. $P_{\rm w}$ is also a time-independent prefactor.

Figures 6(a) and (b) present typical AFM images of water droplets formed in the central part of the sample area, measured rapidly (within about 30 min) after droplet formation resulting from the deposited solution on the NC/TEM grid. A more detailed image of a water droplet is illustrated in figures 6(c) and 6(d). An average diameter of the droplets $D_{\rm d} \approx 0.5$ μm and their average height $h_d \approx 40$–50 nm were obtained. After drying the samples for 7 weeks, the height decreased to $h_d \approx 10$ nm, without a detectable change in $D_{\rm d}$ (figures 7(a), (c) and (d)). The remaining deposit after the complete drying of the droplets consisted of HDA. This was demonstrated via a removal of the HDA deposits from the dry sample by immersing the sample for a period of 5 min in hexane, which is a selective solvent for HDA.

The analysis of the droplet patterns performed by TEM clearly demonstrated that the CoPt$_3$ particles self-assembled into close-packed arrays located at the droplet periphery. For example, figure 7(b) illustrates the TEM image of the droplet shown in figure 7(a). We found that arrays with a different number of nanoparticle chains can be produced via variation of the particle concentration in the initial solution and by generating water droplets of different sizes. For example, figure 8 displays rings composed of several arrays containing mainly 1, 2 or 3 aligned chains of particles, respectively. The particle arrays shown in figure 8(a) were produced with a concentration of 2.4×10^{12} cm^{-3} of CoPt$_3$ particles in solution, and those shown in figures 8(c) and (e) with a concentration of 3.1×10^{12} cm^{-3}. We found that in our experiments, for constant concentration of water and particles in the initial solution, the average size of the particle rings (size of water droplets) and length of the ordered chains of particles (about 100 nm) were always fairly reproducible.

3.3. Formation of the water droplet pattern

Based on the experimental results described above, we conclude that, during hexane evaporation out of the solution
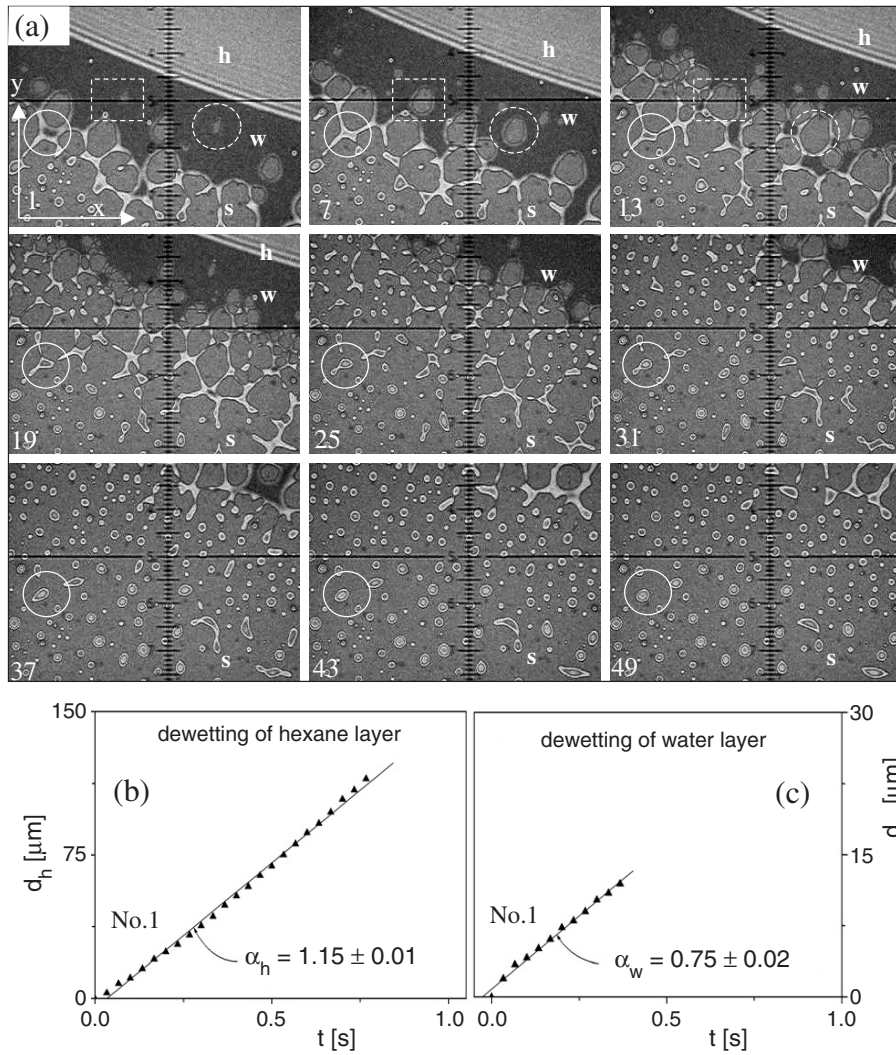
Figure 5. (a) Typical optical micrographs for the retraction of the phase-separated layers of hexane (denoted as h) and water (denoted as w) on the NC/Si substrate (denoted as s). The length of the smallest division (*y* direction) amounts to 5 μm. (b) Time dependence of the dewetted distance for the hexane layer (d_h) on the surface of the water layer along the *y* direction indicated in (a). (c) Time dependence of the dewetted distance for the water layer (d_w) on the surface of the NC layer for hole 1 indicated by the dashed box in (a). The value of α_w for hole 2 indicated by the dashed circle in (a) is similar to that shown for hole 1.

film, the following processes occur: (a) the binary solution film transforms into a double layer composed of a hexane layer on top of a water layer; (b) the hexane layer dewets the surface of the water layer; (c) the particles existing in solution adsorb on the surface of the water layer; (d) if HDA exists in solution, it adsorbs also on the surface of the water layer; (e) the water layer (also when coated with HDA) becomes unstable and decomposes into droplets and (f) during formation of water droplets, the particles located near the droplet edge follow its motion and order along that. Note that many of these events can overlap in time or even take place simultaneously.

The reason for phase separation of the solution layer into a double layer, besides the relative increase in water concentration during evaporation of hexane, is that hexane has a lower surface energy (surface tension $\gamma_h = 18.4$ mN m^{-1}) than water and thus wets the surface region, in order to minimize the free energy at the interface between air and solution [34–37]. On the contrary, water with its comparatively

large surface energy (surface tension $\gamma_0 = 72.5$ mN m^{-1}) accordingly wets the interface between the solution and the substrate. Initially, a hexane layer will spread on water leading to the formation of a neat bilayer, because the spreading coefficient amounts to $S_{h0} = \gamma_0 - \gamma_h - \gamma_{h0} = 3.0$ mN m^{-1} for pure water and hexane [20]. Here, $\gamma_{h0} = 51.1$ mN m^{-1} [32] is the surface tension at the interface between hexane and water. However, at equilibrium, in the resulting bilayer, the top hexane layer is saturated with water and the lower water layer is saturated with hexane. As a result, the value of the equilibrium spreading coefficient becomes $S_{h0} \leqslant 0$. The change from a positive initial spreading coefficient to a negative equilibrium spreading coefficient is a well-known phenomenon for short alkanes spreading on water [38–40]. We found that the experimentally observed time dependence of the dewetted distance of the hexane layer can be described as $d_h(t) \sim t^{\alpha_h}$ with $\alpha_h \approx 1$ (figure 5(a)). Such dependence corresponds to dewetting where the driving capillary forces
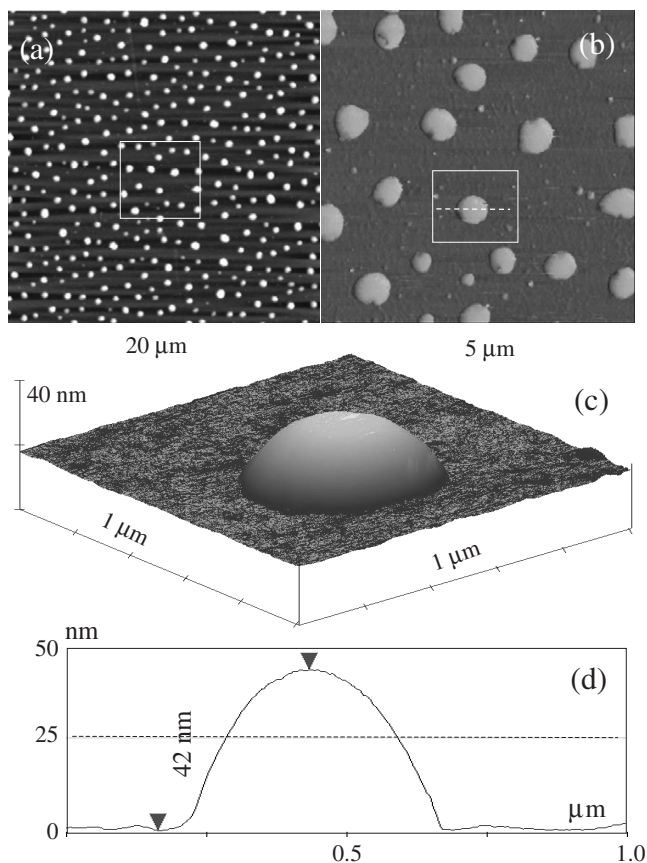
Figure 6. Tapping-mode AFM measurements: (a) height image of water droplets located on a nitrocellulose film measured directly after spreading of the solution; (b) magnified phase image of an area indicated by the square box (solid line) in (a); (c) magnified three-dimensional image of a water droplet indicated by the box in (b); (d) profile analysis of the scan along the dashed line indicated in (b).
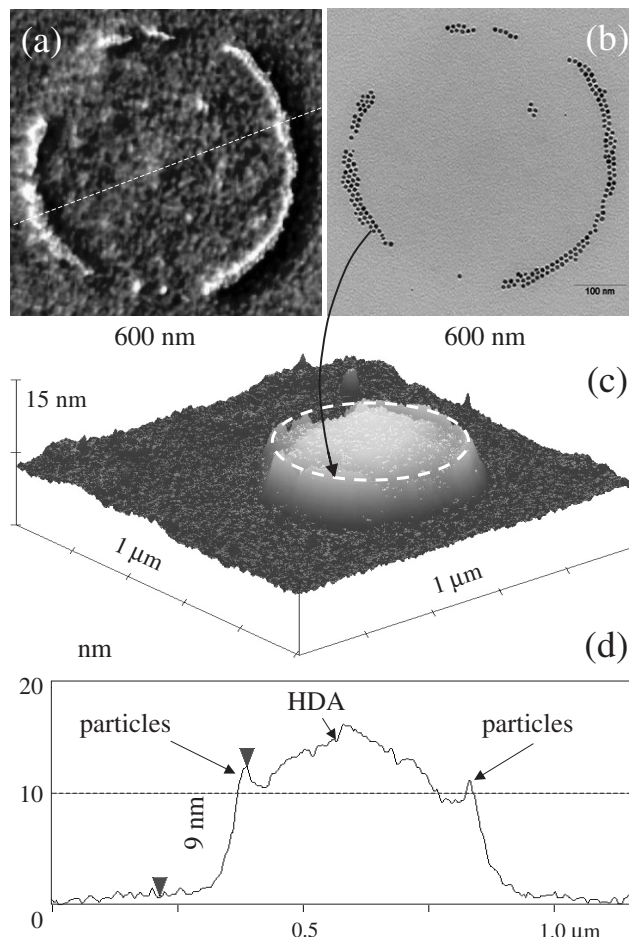

Figure 7. (a) Tapping-mode AFM height image of a water droplet located on an NC/TEM grid measured after drying the samples for 7 weeks. (b) Corresponding TEM image of the same droplet shown in (a). (c) Three-dimensional image of a droplet shown in (a). The indicated dashed ring illustrates the location of a nanoparticle ring shown in (b). (d) Profile analysis of the scan along the dashed line indicated in (a).

(uncompensated Young force) are balanced by viscous forces (forces per unit length of the three-phase contact line) [41, 42]. In this case, i.e. for nonslipping films, the energy is dissipated in a small volume located at the contact line [8] and the dewetting velocity remains constant [42].

The thickness of the water layer initially formed in the middle part of the sample area can be determined from the initial volume of the water droplets. For example, in figure 6(a), 81 droplets are located on an area of 10×10 μm^2. The corresponding thickness of the water layer amounts to about 3 nm. Deduced from the concentration of water in solution (0.015 vol%), an on average 11 nm thick water layer was expected. This difference can be explained firstly by the evaporation of water during the time span between the initial deposition of the solution and the AFM measurements. Secondly, the thickness of the water layer at the edge of the sample area was larger than in the central part. A water layer located on an NC-coated substrate is unstable and starts to dewet by forming holes, because the spreading coefficient S_{01} is negative, $S_{01} = \gamma_1 - \gamma_0 - \gamma_{01} = -89$ mN m^{-1} [20]. Here, $\gamma_1 = 38$ mN m^{-1} designates the surface tension of NC (at the boundary to air); $\gamma_{01} = 55$ mN m^{-1} is the interfacial tension

between water and NC. The latter was calculated following Israelachvili [15] as $\gamma_{01} = \gamma_0 + \gamma_1 - 2(\gamma_{0d}\gamma_1)^{0.5}$, where $\gamma_{0d} = 20$ mN m^{-1} is only the dispersion force contribution to the surface tension of water. The value of S_{01} estimated above for pure water on the NC film should only be considered rather as a qualitative indicator. When this thin water layer is covered with HDA, the reduction of γ_0 and γ_{01} have to be taken into account. We found that the experimental time dependence of the dewetted distance of the water layer can be described as $d_w(t) \sim t^{\alpha_w}$ with $\alpha_w \approx 0.7$. Such dependence reflects the dewetting of a slipping film, where the capillary energy is dissipated over the entire moving part of the film and being proportional to the width of the rim collecting the liquid originating from the dewetted region [41, 43–46].

The experimentally determined volume of the HDA deposit, which is expected to be adsorbed on the surface of the water layer after hexane evaporation, can be translated into a continuous film of about 0.8 nm thickness. Deduced from the concentration of HDA in solution (0.001 vol%), a layer of about 0.8 nm thick was expected on average, which is thus in
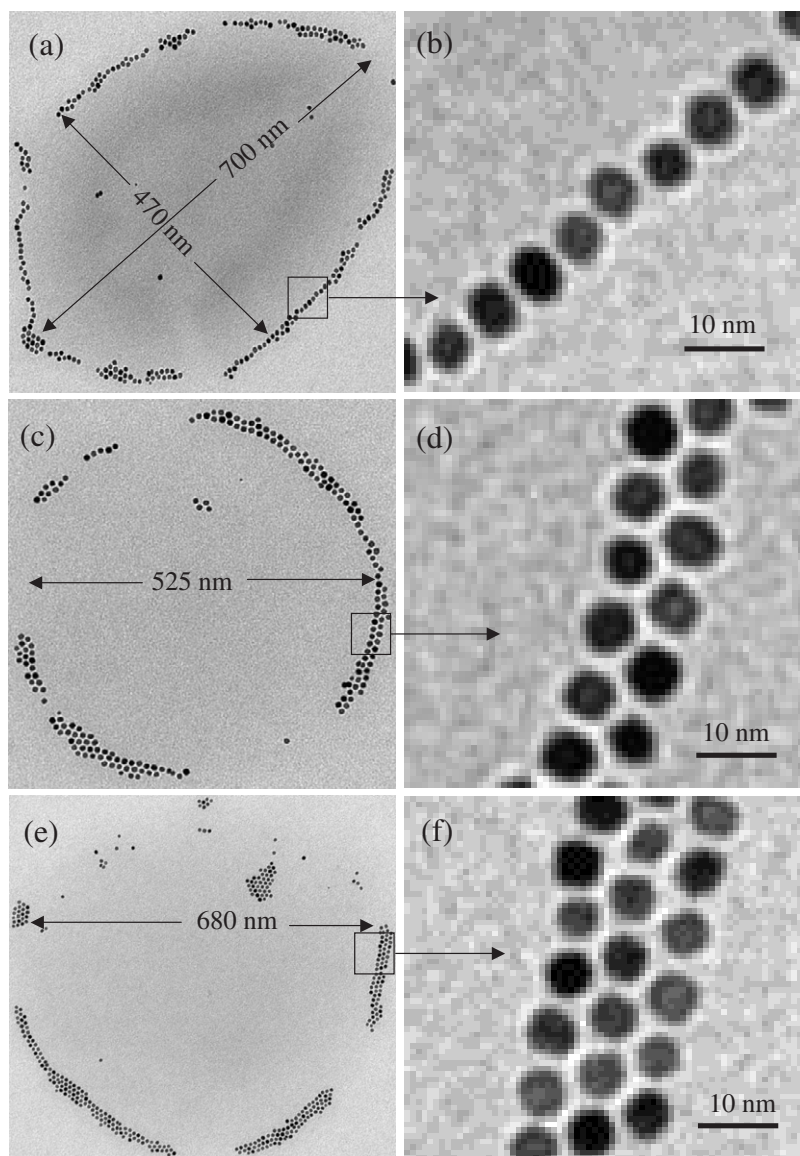
Figure 8. (a) TEM image of CoPt$_3$ ring composed of several arrays containing mainly one chain. (b) Magnified image of an area indicated by the square box in (a). (c) TEM image of CoPt$_3$ ring composed of several arrays containing mainly two chains. (d) Magnified image of an area indicated by the square box in (c). (e) TEM image of CoPt$_3$ ring composed of several arrays containing mainly three chains. (f) Magnified image of an area indicated by the square box in (e).

good agreement with the value estimated experimentally. The HDA molecules can adsorb on the water surface either as a monolayer with a discrete thickness of 1.4 nm (length of HDA molecule) or as micelles with thickness of 2.8 nm (2 ML) [47]. Accordingly, we conclude that only about 57% of the water surface can be covered with a 1.4 nm thick HDA layer. If HDA forms micelles on the water layer, the covered area will even be smaller. The nanoparticles (figure 7(b)) can only cover less than 1% of the planar water surface. This situation changes significantly when the planar water layer deforms to the water droplets. In this case, HDA has to cover the surface of the water droplet with a continuous film of about 5 nm thickness. During evaporation of water from the droplet, its surface area decreases and, finally, HDA yields a droplet-like deposit whose thickness amounts to about 10 nm (see figure 7(d)).

3.4. Scenario for the nanoparticle array formation

Taking into account the results described above, figure 9 sketches a schematic scenario of the mechanism we propose as being responsible for the formation of the close-packed arrays of nanoparticles. Figure 9(a) schematically shows the dewetting of a hexane layer on top of the water layer. During dewetting and evaporation of hexane, most of the nanoparticles and HDA contained in the solution adsorb on the water surface. As the diameter of the CoPt$_3$ particles coated with the HDA monolayer (stabilizer) amounts to 8.8 nm, and thus is larger than the thickness of the water layer (or comparable), the nanoparticles could contact the NC/substrate. During the growth of dewetting holes in the water layer, the removed water accumulates at the edge of the holes and builds the rims (figure 9(b)). A cross section of the rim can be
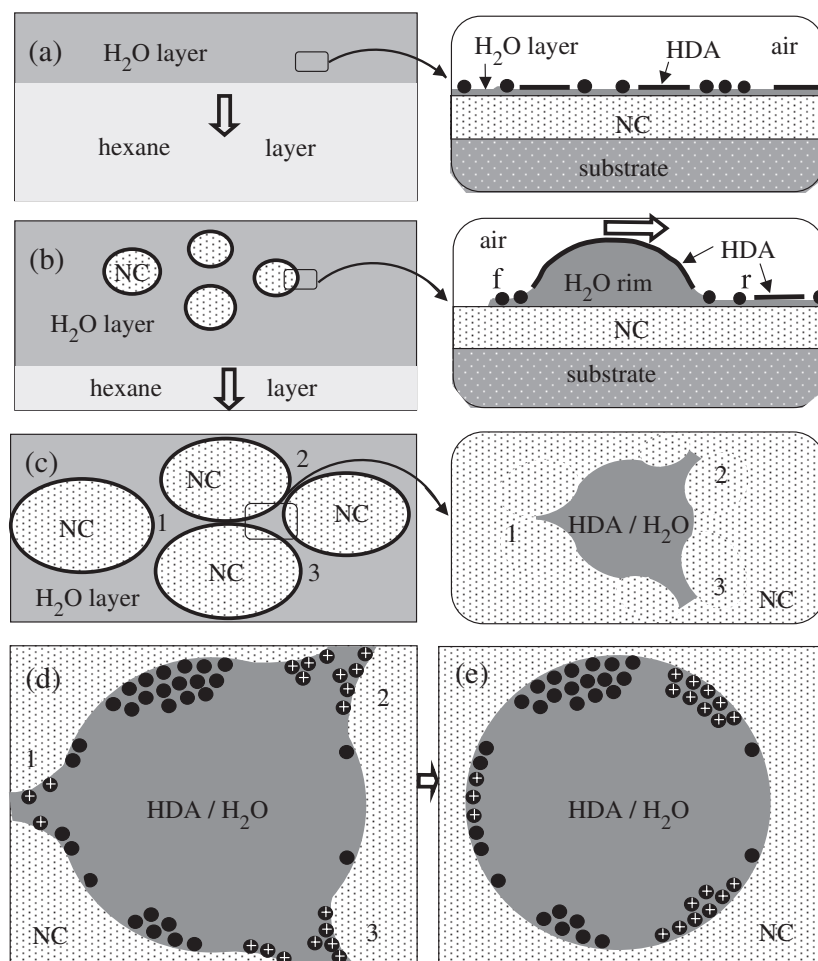
Figure 9. Schematic illustration of the development of close-packed particle arrays via the dewetting water layer. (a) Top view of the water layer formed on the NC-coated substrate after dewetting and evaporation of hexane. Magnified side view of an area indicated by the square box is shown on the right. The particles are denoted as circles and the HDA clusters as plates. (b) Development of the holes appearing in the dewetting water layer. Magnified side view of the rim forming in the dewetting water layer is shown on the right; f and r denote front and rear sides of the rim. (c) Formation of the cellular structure containing water ribbons. Formation of a water droplet from a fragment indicated by the square box is shown on the right. (d) Assembling of particles at the water droplet edge. The particles located at the ribbon edges are additionally denoted with white crosses. (e) Final formation of water droplet with particles assembled at its edge.

approximated as a portion of a circle. Because the front side of the rim is moving, the particles close to the contact line have to follow its retraction and, consequently, assemble into the close-packed arrays along that line. When the holes become large enough so that their rims coalesce (figure 9(c)), this results in the formation of ribbons which assemble into the cellular (polygonal) structure. These ribbons are unstable (Rayleigh instability) and decompose into droplets. According to experimental results, most of the particles which were collected from the dewetted area assemble at the contact lines of the water droplets (figure 9(d)). Finally, the force governing the arrangement of particles into ordered assemblies is the capillary attraction, since the thickness of the water layer at the droplet edge is comparable to the particle diameter [48] (figure 9(e)).

In summary, it has been demonstrated experimentally that, during evaporation from a thin film of a hexane solution also containing CoPt$_3$ particles, HDA, and water, the following processes occur. The initial solution film transforms into a

double layer containing a hexane layer on top of a water layer. The hexane layer dewets the surface of the water layer. After dewetting and evaporation of the hexane layer, the particles and HDA adsorb on the water layer. The water layer coated with HDA and nanoparticles gets unstable and decomposes into droplets. During formation of water droplets, the particles located close to the droplet edge follow its retraction and order along the contact line.

3.5. Nanoparticle arrays for electronic transport studies: an outlook

The self-assembly of nanoparticles is one of the most promising basic approaches to produce low-dimensional composite materials with novel properties. During the past few years, electronic properties of individual particles [49] as well as those of two- and three-dimensional arrays have been studied extensively [50–52]. Recently, electronic transport through quasi-one-dimensional arrays of nanoparticles (containing four

chains of particles; particle diameter 5.5 nm) was experimentally investigated [53]. So far, no experimental studies are available on truly one-dimensional (1D) arrays of particles (containing only one or two chains). Thus, the arrays presented here (see figure 8) represent quite promising objects for such studies.

The ordering of nanoparticles to regular 1D structures was reported in several papers. Wyrwa *et al* [54] described the 1D arrangements of metal nanoparticles formed by self-assembly processes at the phase boundary between water and dichloromethane. Huang *et al* [55] showed that the 1D chains of single-particle thickness can be readily deposited on a substrate from a dilute Langmuir–Blodgett particle monolayer via a stick–slip motion of the water–substrate contact line. Suematsu *et al* [56] observed that nanoparticles self-assembled into ring-shaped structures that contain two, three or more particle chains, prepared by casting a toluene solution doped with polystyrene and Ag nanoparticles. Khanal *et al* [57] found that gold nanorods dispersed in dichloromethane can be organized into 1D circular arrays around the circumferences of water droplets located on the surface of the solution film.

Our work demonstrates a simple preparation procedure which provides for a new possibility for fabricating ordered one-dimensional structures of nanoparticles in a controllable and cost-effective manner. The nanoparticle arrays prepared in the present work can be used, for example, for the study of the electronic hopping transport in an one-dimensional array of nanoparticles.

4. Conclusion

Spin-coating suspensions or solutions represents a simple way for depositing nanoparticles or solid aggregates onto solid supports. It is possible to introduce various self-assembly processes which are driven by evaporation of the solvent. In the examples presented here, we demonstrate several possibilities and some advantages provided by using binary solutions. In particular, when one of the solvents evaporates faster than the other, this represents a way of depositing nanoparticles or aggregates onto the surface of a thin fluid layer. Compared to deposition onto a solid substrate, these particles can float on a fluid surface and thus move more easily due to lower frictional resistance. Moreover, instabilities and dewetting processes of the supporting fluid layer provide ways for arranging these particles into (ordered) arrays. It is also feasible to form nano-objects (small polymer aggregates or crystals) during evaporation of one solvent if, for example, the polymer forming these aggregates is only soluble in the faster evaporating solvent. Probably the most important advantage is that the whole deposition and assembly process is fast (it may take only a few seconds). The use of binary solutions or suspensions also offers a highly versatile approach due to the interplay of phase separation, evaporation, dewetting and fingering or Rayleigh instabilities. In addition, by varying the concentration of solutes, the volume ratio of solvents, the difference in volatility, surface and interfacial tensions or the substrate properties these processes and instabilities can be tuned. We hope that further research will allow us to identify

under which combination of the above parameters the self-assembly process of solute nanoparticles and aggregates can be optimized.

References

[1] Reiter G 1992 *Phys. Rev. Lett.* **68** 75
[2] Limaye A V, Narhe R D, Dhote A M and Ogale S B 1996 *Phys. Rev. Lett.* **76** 3762
[3] Thiele U, Merting M and Pompe W 1998 *Phys. Rev. Lett.* **80** 2869
[4] Mougin K and Haidara H 2002 *Langmuir* **18** 9566
[5] Seemann R, Herminghaus S, Neto C, Schlagowski S, Podzimek D, Konrad R, Mantz H and Jakobs K 2005 *J. Phys.: Condens. Matter* **17** S267
[6] Vrij A 1996 *Discuss. Faraday Soc.* **429** 23
[7] Vrij A and Overbeek J Th G 1968 *J. Am. Chem. Soc.* **90** 3074
[8] de Gennes P G 1985 *Rev. Mod. Phys.* **57** 827
[9] Brochard-Wyart F and Daillant J 1990 *Can. J. Phys.* **68** 1084
[10] Oron A, Devis S H and Bankoff S G 1997 *Rev. Mod. Phys.* **69** 931
[11] Sharma A and Khanna R 1998 *Phys. Rev. Lett.* **81** 3463
[12] Samid-Merzel N, Lipson S G and Tannhauser D S 1998 *Phys. Rev. E* **57** 2906
[13] de Gennes P G 2001 *Eur. Phys. J. E* **6** 421
[14] de Gennes P G 2002 *Eur. Phys. J. E* **7** 31
[15] Israelachvili J N 1991 *Intermolecular and Surface Forces* (London: Academic)
[16] Pototsky A, Bestehorn M, Merkt D and Thiele U 2004 *Phys. Rev. E* **70** 025201(R)
[17] Pototsky A, Bestehorn M, Merkt D and Thiele U 2005 *J. Chem. Phys.* **122** 224711
[18] Govor L V, Reiter G, Parisi J and Bauer G H 2004 *Phys. Rev. E* **69** 061609
[19] Govor L V, Parisi J, Bauer G H and Reiter G 2005 *Phys. Rev. E* **71** 051603
[20] Adamson A W 1982 *Physical Chemistry of Surfaces* (New York: Wiley)
[21] Govor L V, Reiter G, Bauer G H and Parisi J 2006 *Phys. Rev. E* **74** 061603
[22] Defay R, Prigogine I, Bellemans A and Everett D H 1966 *Surface Tension and Adsorption* (London: Longmans Green)
[23] Ober R, Paz L, Taupin C, Pincus P and Boileau S 1983 *Macromolecules* **16** 50
[24] di Meglio J M, Ober R, Paz L, Taupin C, Pincus P and Boileau S 1983 *J. Physique* **44** 1035
[25] Karthaus O, Koito T and Shimomura M 1999 *Mater. Sci. Eng.* C **8/9** 523
[26] Troian S M, Herbolzheimer E and Safran S A 1990 *Phys. Rev. Lett.* **65** 333
[27] Rayleigh L 1878 *Proc. London Math. Soc.* **10** 4
[28] Eggers J 1997 *Rev. Mod. Phys.* **69** 865
[29] Edmond K V, Schofield A B, Marquez M, Rothstein J P and Dinsmore A D 2006 *Langmuir* **22** 9052
[30] Weh L 2004 *J. Colloid Interface Sci.* **271** 407
[31] Shevchenko E, Talapin D, Kornowski A, Rogach A and Weller H 2002 *J. Am. Chem. Soc.* **124** 11480
[32] Demond A H and Lindner A S 1993 *Environ. Sci. Technol.* **27** 2318

[33] Govor L V, Reiter G, Bauer G H and Parisi J 2007 *Phys. Rev.* E **76** 041609
[34] Bruder F and Brenn R 1992 *Phys. Rev. Lett.* **69** 624
[35] Steiner U, Klein J and Fetters L J 1994 *Phys. Rev. Lett.* **72** 1498
[36] Straub W, Bruder F, Brenn R, Krausch G, Bielefeldt H, Kirsch A, Marti O, Mlynek J and Marko J F 1995 *Europhys. Lett.* **29** 353
[37] Tanaka K, Takahara A and Kajiyama T 1996 *Macromolecules* **29** 3232
[38] Hirasaki G J 1993 *J. Adhes. Sci. Technol.* **7** 285
[39] Kneafsey T J and Hunt J R 2004 *J. Contam. Hydrol.* **68** 143
[40] Dobbs H and Bonn D 2001 *Langmuir* **17** 4674
[41] Brochard-Wyart F, Martin P and Redon C 1993 *Langmuir* **9** 3682
[42] Redon C, Brochard-Wyart F and Rondelez F 1991 *Phys. Rev. Lett.* **66** 715
[43] Brochard-Wyart F, de Gennes P G, Hervert H and Redon C 1994 *Langmuir* **10** 1566
[44] Redon C, Brzoska J B and Brochard-Wyart F 1994 *Macromolecules* **27** 468
[45] Reiter G, Auroy P and Auvray L 1996 *Macromolecules* **29** 2150

[46] Reiter G and Khanna R 2000 *Phys. Rev. Lett.* **85** 2753
[47] Govor L V, Reiter G, Bauer G H and Parisi J 2006 *Phys. Lett.* A **353** 198
[48] Kralchevsky P A, Denkov N D, Paunov V N, Velev O D, Ivanov I B, Yoshimora H and Nagayama K 1994 *J. Phys.: Condens. Matter* **6** A395
[49] Delft J and Ralf D C 2001 *Phys. Rep.* **345** 61
[50] Yu D, Wang C J, Wehrenberg B L and Guyot-Sionnest P 2004 *Phys. Rev. Lett.* **92** 216802
[51] Morgan N Y, Leatherdale C A, Drndic M, Jarosz M V, Kastner M A and Bawendi M 2002 *Phys. Rev.* B **66** 075339
[52] Parthasarathy R, Lin X M and Jaeger H M 2001 *Phys. Rev. Lett.* **87** 186807
[53] Elteto K, Lin X M and Jaeger H M 2005 *Phys. Rev.* B **71** 205412
[54] Wyrwa D, Beyer N and Schmid G 2002 *Nano Lett.* **2** 419
[55] Huang J, Tao A R, Connor S, He R and Yang P 2006 *Nano Lett.* **6** 524
[56] Suematsu N J, Ogawa Y, Yamamoto Y and Yamaguchi T 2007 *J. Colloid Interface Sci.* **310** 648
[57] Khanal B P and Zubarev E R 2007 *Angew. Chem.* **119** 2245